

**The following resources related to this article are available online at [www.sciencemag.org](http://www.sciencemag.org) (this information is current as of November 16, 2009):**

**Updated information and services**, including high-resolution figures, can be found in the online version of this article at:

<http://www.sciencemag.org/cgi/content/full/326/5955/977>

**Supporting Online Material** can be found at:

<http://www.sciencemag.org/cgi/content/full/326/5955/977/DC1>

This article appears in the following **subject collections**:

Materials Science

[http://www.sciencemag.org/cgi/collection/mat\\_sci](http://www.sciencemag.org/cgi/collection/mat_sci)

Information about obtaining **reprints** of this article or about obtaining **permission to reproduce this article** in whole or in part can be found at:

<http://www.sciencemag.org/about/permissions.dtl>

# A Strain-Driven Morphotropic Phase Boundary in BiFeO<sub>3</sub>

R. J. Zeches,<sup>1\*</sup> M. D. Rossell,<sup>2</sup> J. X. Zhang,<sup>1</sup> A. J. Hatt,<sup>3</sup> Q. He,<sup>4</sup> C.-H. Yang,<sup>4</sup> A. Kumar,<sup>5</sup> C. H. Wang,<sup>7</sup> A. Melville,<sup>5,6</sup> C. Adamo,<sup>5,6</sup> G. Sheng,<sup>5</sup> Y.-H. Chu,<sup>7</sup> J. F. Ihlefeld,<sup>5,6</sup> R. Erni,<sup>2</sup> C. Ederer,<sup>8</sup> V. Gopalan,<sup>5</sup> L. Q. Chen,<sup>5</sup> D. G. Schlom,<sup>6</sup> N. A. Spaldin,<sup>3</sup> L. W. Martin,<sup>9,10</sup> R. Ramesh<sup>1,4,9</sup>

Piezoelectric materials, which convert mechanical to electrical energy and vice versa, are typically characterized by the intimate coexistence of two phases across a morphotropic phase boundary. Electrically switching one to the other yields large electromechanical coupling coefficients. Driven by global environmental concerns, there is currently a strong push to discover practical lead-free piezoelectrics for device engineering. Using a combination of epitaxial growth techniques in conjunction with theoretical approaches, we show the formation of a morphotropic phase boundary through epitaxial constraint in lead-free piezoelectric bismuth ferrite (BiFeO<sub>3</sub>) films. Electric field-dependent studies show that a tetragonal-like phase can be reversibly converted into a rhombohedral-like phase, accompanied by measurable displacements of the surface, making this new lead-free system of interest for probe-based data storage and actuator applications.

Modern functional materials, for example ferromagnets and piezoelectrics, are typically chemically complex and exhibit the coexistence of multiple phases that evolve as a consequence of chemical alloying (1, 2). In such materials, huge responses to external stimuli are often found at phase boundaries (3). In the past two decades, examples of the discovery of such behavior include the emergence of colossal magnetoresistance in doped manganites, high-temperature superconductivity in doped cuprates, and large piezoelectric responses in relaxor ferroelectrics (4). The large piezoelectric coefficients in Pb(Zr<sub>x</sub>Ti<sub>1-x</sub>)O<sub>3</sub> (PZT), Pb(Mg<sub>0.33</sub>Nb<sub>0.67</sub>)O<sub>3</sub>-PbTiO<sub>3</sub> (PMN-PT), and Pb(Zn<sub>0.33</sub>Nb<sub>0.67</sub>)O<sub>3</sub>-PbTiO<sub>3</sub> (PZN-PT) systems, for example, occur in compositions that lie at the boundary between two crystal structures, for example, a rhombohedral-to-tetragonal phase boundary (5–8). These giant piezoelectric responses have made PZT, PMN-PT, and PZN-PT the materials of choice for a variety of applications ranging from micropositioners to acoustic sensing in sonar. Notwithstanding the dramatic progress in the development of functional piezoelectric devices from these lead-based perovskites, two broad questions

remain: (i) are there lead-free alternatives to the above-mentioned systems, and (ii) are there viable alternative pathways that are fundamentally different from the chemical alloying approaches (such as that seen in the PZT and PMN-PT systems) to achieve large piezoelectric responses? In this report, we demonstrate that epitaxial strain can be used to drive the formation of a morphotropic phase boundary and create large

piezoelectric responses in lead-free ferroelectric materials.

BiFeO<sub>3</sub> (BFO) is a multiferroic perovskite that exhibits antiferromagnetism coupled with ferroelectric order (9, 10). The structural stability of the parent rhombohedral phase of this material has been the focus of a number of theoretical studies (11, 12). Although the parent ground state is a rhombohedrally distorted perovskite (*R3c*), a tetragonally distorted perovskite phase (*P4mm* symmetry, with in-plane lattice parameter *a* ~ 3.665 Å and out-of-plane lattice parameter *c* ~ 4.655 Å) with a large spontaneous polarization has been identified (11, 13, 14). We use the “T” notation in reference to a parent tetragonal phase with *P4mm* symmetry that has a *c* axis lattice parameter of ~4.65 Å and encompasses small monoclinic distortions from this tetragonal symmetry. Similarly, we use the “R” notation in reference to a distorted form of the *R3c* parent phase that has a *c* axis lattice parameter of ~4.0 Å. It has been established that that strain is particularly effective in altering the stable crystal structure of thin films where strains of several percent can be imparted through commensurate epitaxial growth on an underlying substrate (15). We show that epitaxial strain can be used to stabilize a tetragonal polymorph of BFO and that intermediate strains position BFO on a morphotropic phase transition between its T and R polymorphs.

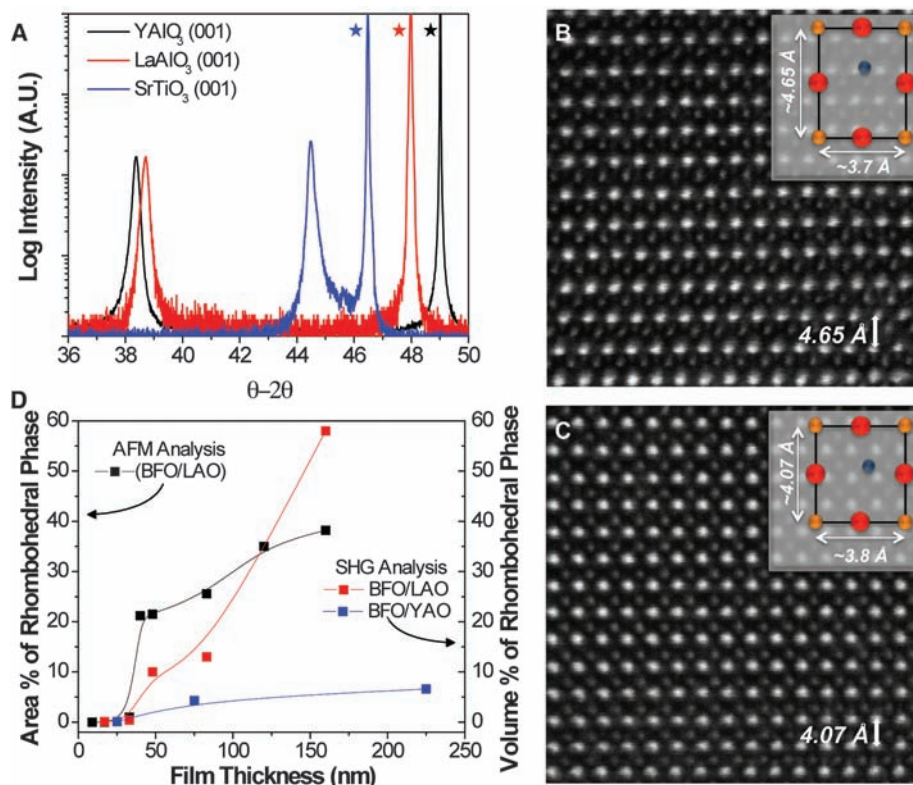


**Fig. 1.** (A) X-ray diffraction of the pseudocubic 002-diffraction peak of BFO/STO (001), BFO/LAO(001), and BFO/YAO(110) shows the presence of a long-axis T phase on both LAO and YAO substrates. Substrate peaks are marked with a star. (B and C) Atomic resolution STEM images of the T phase and the R phase, respectively. Insets show schematic illustration of the unit cell. (D) The evolution of the structure with thickness, including the area fraction (left axis) and the volume fraction of the R phase.

<sup>1</sup>Department of Materials Science and Engineering, University of California, Berkeley, Berkeley, CA 94720, USA.

<sup>2</sup>National Center for Electron Microscopy, Lawrence Berkeley National Laboratory, Berkeley, CA 94720, USA.

<sup>3</sup>Materials Department, University of California, Santa Barbara, Santa Barbara, CA 93106, USA.

<sup>4</sup>Department of Physics, University of California, Berkeley, Berkeley, CA 94720, USA.

<sup>5</sup>Department of Materials Science and Engineering, Pennsylvania State University, State College, PA 16802, USA.

<sup>6</sup>Department of Materials Science and Engineering, Cornell University, Ithaca, NY 14853, USA.

<sup>7</sup>Department of Materials Science and Engineering, National Chiao Tung University, HsinChu, Taiwan 30010.

<sup>8</sup>School of Physics, Trinity College Dublin, College Green, Dublin 2, Ireland.

<sup>9</sup>Materials Science Division, Lawrence Berkeley National Laboratory, Berkeley, CA 94720, USA.

<sup>10</sup>Department of Materials Science and Engineering, University of Illinois, Urbana-Champaign, Urbana, IL 61822, USA.

\*To whom correspondence should be addressed. E-mail: rzeches@berkeley.edu

After establishing the characteristics of the pure T polymorph, we show that the T and R phases can coexist on a length scale of tens of nanometers in films grown with intermediate strain and have huge piezoelectric responses.

We grew epitaxial BFO films using conventional molecular beam epitaxy (MBE) and laser-MBE on single-crystal substrates of (001) LaAlO<sub>3</sub> (LAO) (rhombohedral with a pseudocubic lattice parameter  $a = 3.79$  Å) and (110) YAlO<sub>3</sub> (YAO) (orthorhombic with a pseudocubic lattice parameter  $a = 3.69$  Å). Reference rhombohedral polymorphs of BFO were grown on (001) SrTiO<sub>3</sub> (STO) (cubic with lattice parameter  $a = 3.905$  Å) substrates. For electrical and piezoresponse force microscopy (PFM) studies only, a 3- to 50-nm layer of epitaxial La<sub>0.5</sub>Sr<sub>0.5</sub>CoO<sub>3</sub> (LSCO) ( $a = 3.82$  Å) or La<sub>0.7</sub>Sr<sub>0.3</sub>MnO<sub>3</sub> (LSMO) ( $a = 3.85$  Å) was used as a bottom electrode. Detailed structural characterization was completed by a combination of x-ray diffraction, reciprocal space mapping, and scanning transmission electron microscopy–based atomic imaging (TEAM 0.5 at the National Center for Electron Microscopy). Ferroelectric domains were imaged and switched using PFM as described previously (16). Local surface displacements

were measured using high-resolution atomic force microscopy (AFM) as a function of applied DC field.

These measurements of the structural aspects of the T phase and its evolution with thickness were completed without a bottom electrode in order to understand the direct influence of epitaxial constraint on the phase evolution. Figure 1A shows a typical  $\theta$ – $2\theta$  scan of BFO films grown on LAO, YAO, and STO substrates. The films grown on the reference STO substrate show the same monoclinically distorted rhombohedral structure that is established in the literature (17–20). In contrast, the films grown on LAO and YAO exhibit strong reflections at  $2\theta$  values corresponding to an out-of-plane lattice parameter of  $\sim 4.65$  Å. Detailed reciprocal space mapping scans as a function of film thickness reveal a number of interesting aspects (21). First, for thinner films on LAO substrates (less than  $\sim 50$  nm), we measure the in-plane lattice parameters to be  $a \sim 3.84$  Å and  $b \sim 3.76$  Å, respectively. (See fig. S1 for reciprocal space map data used to determine these lattice constants.) Second, we observe a monoclinic tilt of the structure with  $\beta \sim 88.6^\circ$ . On the other hand, for thicker films ( $>50$  nm) we

observe the coexistence of the two phases. The insets of Fig. 1, B and C schematically describe the T and R phases discussed throughout this report.

The atomic structure of these two phases was imaged directly using the TEAM 0.5 transmission electron microscope (21). Atomic resolution high-angle annular dark-field scanning transmission electron microscopy (HAADF-STEM) images, also referred to as Z-contrast images, of these two different phases are shown in Fig. 1, B and C, respectively. Both images were acquired along the perovskite pseudocubic direction and exhibit atomic columns with two distinct intensities, with the Bi atom columns appearing brighter than the Fe atom columns. The strong atomic-number contrast of HAADF-STEM prevents the observation of the oxygen atomic columns next to the cation-containing columns (22). It is interesting to note that the small size of the aberration-corrected electron probe ( $\sim 0.6$  Å) used for the HAADF-STEM imaging and the high mechanical and electrical stability of the microscope employed allowed for resolving the displacement of the Fe atoms from the center of the unit cell defined by Bi rectangles. The electron diffraction patterns and the Fourier transforms in fig. S2, obtained from the images in Fig. 1, B and C, reveal clear differences between the symmetries of the T and R phases.

As the films are made thicker, we observe the emergence of the R phase that coexists with the T phase. The relative areal and volume fractions of these two phases as a function of film thickness are shown for films on both LAO and YAO substrates in Fig. 1D. Areal fractions were calculated from detailed high-resolution AFM studies of the surface, shown in fig. S3, while second harmonic generation (SHG) studies shown in fig. S4 give volumetric fractions (21). As expected, in the case of films grown on YAO (the substrate with the smallest lattice mismatch with the T phase), we observe that the film remains essentially tetragonal-like for the range of thicknesses studied. In contrast, films grown on LAO show a distinct evolution of the phase mixture due to relaxation of the epitaxial strain with increased thickness.

Let us now turn our attention to understanding the atomic structure of this morphotropic phase boundary-like interface in the mixed phase. High-resolution AFM images (Fig. 2A) show a characteristic striped contrast that we attribute to the mixed phase. From such images, the spacing of the stripes is measured to be  $\sim 30$  to 50 nm, with a peak-to-valley height difference of 1 to 2 nm (Fig. 2B). We then carried out low- and high-resolution transmission electron microscopy (TEM) studies of this mixed phase region. Figure 2C shows a typical low-magnification TEM image of the portion of the sample that exhibits the striped contrast. The spacing of the stripes in this image is commensurate with that obtained in the AFM image, that is, 30 to 50 nm. Higher-resolution atomic imaging (carried out on the TEAM 0.5 microscope) reveals the structural details of this mixed phase (Fig. 2D), in which the T phase is inter-

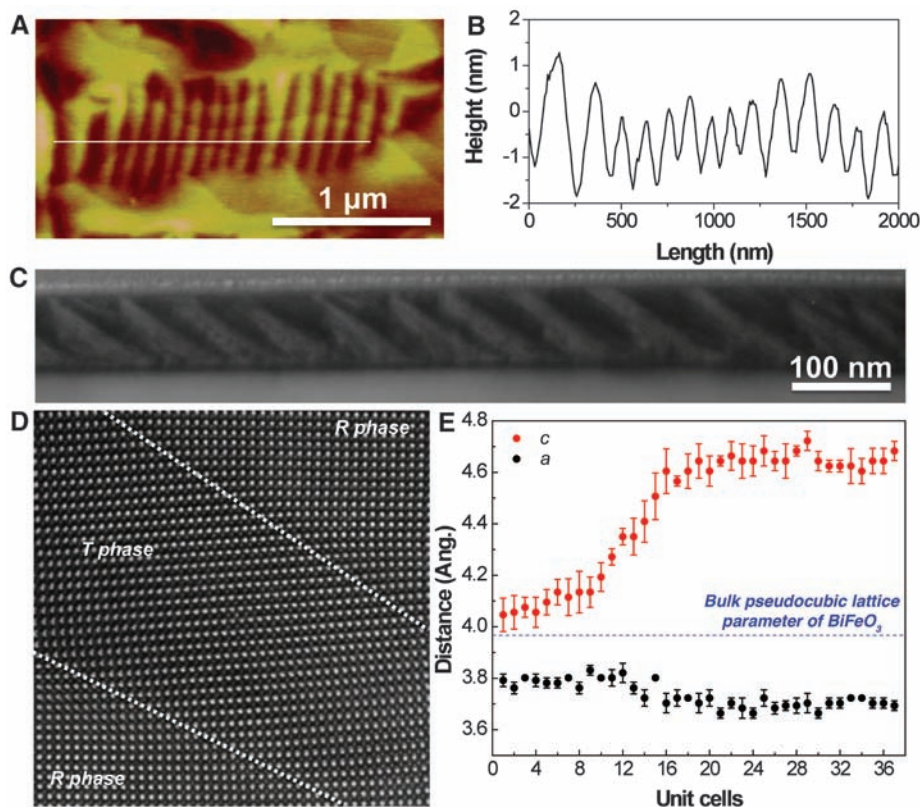


**Fig. 2.** (A) High-resolution AFM image of a mixed phase region. (B) Corresponding line trace at white line in (A) demonstrates  $\sim 2$ - to 3-nm height changes going from the T (bright) to R (dark) phase. (C) Low-resolution cross-sectional TEM image of a mixed phase region in an 85-nm-thick BFO/LAO film. Here, the light areas correspond to the T phase and the dark areas to the R phase. (D) High-resolution TEM image of the boundaries between R and T regions, indicated by dashed lines. A smooth transition between phases is observed; no dislocations or defects are found at the interface. (E) Corresponding in-plane ( $a$ , black) and out-of-plane ( $c$ , red) lattice parameters (mean  $\pm$ SD) demonstrate nearly a 13% change in the out-of-plane lattice parameter in just under 10 unit cells.

persed between two R phase regions. The structure changes smoothly from the T phase to the R phase over a distance of  $\sim 10$  unit cells, as shown in Fig. 2E. Specifically, the out-of-plane lattice parameter changes from  $4.06 \text{ \AA}$  in the R phase to  $4.65 \text{ \AA}$  in the T phase without the insertion of misfit dislocations. The in-plane lattice parameter is constrained by the substrate lattice parameter and changes slightly (from  $\sim 3.8 \text{ \AA}$  in the R phase to  $\sim 3.7 \text{ \AA}$  in the T phase). Thus, the  $c/a$  ratio changes from 1.07 for the R phase to 1.27 in the T phase in just over 10 unit cells.

To understand the observed coexistence of T and R phases, we performed density functional calculations within the local density approximation plus the Hubbard parameter  $U$  (LDA+ $U$ ) approximation ( $U_{\text{eff}} = U - J = 2 \text{ eV}$ ), using the projector augmented wave (PAW) method as implemented in the Vienna ab initio simulation package (VASP) (23, 24). We use a monoclinic 10-atom unit cell, which allows the structure to continuously change from the rhombohedral  $R3c$  symmetry of bulk BFO to the  $P4mm$  tetragonal symmetry studied in earlier theoretical work (11). We employ a 5 by 5 by 5  $k$ -point sampling and a plane wave energy cut-off of 550 eV, and assume the G-type antiferromagnetic ordering of bulk BFO. To simulate the effect of epitaxial strain, we constrain the unit cell lattice vectors in the pseudocubic (001) plane and relax the out-of-plane cell parameter and all internal coordinates by minimizing the Hellman-Feynman forces to a tolerance of  $0.005 \text{ eV/\AA}$ . The internal coordinates are initialized corresponding to monoclinic  $Cc$  symmetry. The results for compressive strain are shown in Fig. 3, A and B. Strains are given relative to the LDA+ $U$  equilibrium lattice parameter  $a = 3.89 \text{ \AA}$  of bulk  $R3c$  BFO.

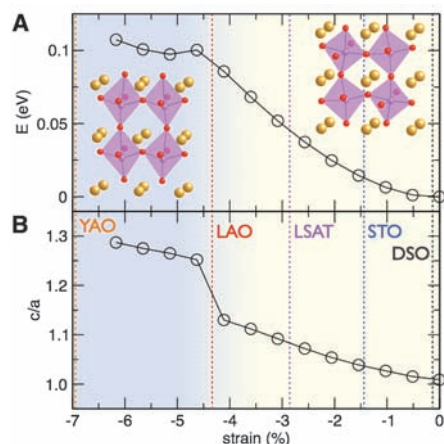


**Fig. 3.** (A) Evolution of the energy of the BFO structure as a function of in-plane strain. (B) Evolution of the  $c/a$  lattice parameter ratio as a function of strain for BFO. These data show the presence of two phases—both with monoclinic symmetry—the long-axis T phase (left) and the short-axis R phase. The lattice mismatches between a number of commonly used and tested oxide substrates are shown as dashed lines.

We find that for a compressive strain, around 4.5% BFO undergoes a strain-induced iso-symmetric structural transformation (25) that is accompanied by an abrupt increase in  $c/a$  ratio (Fig. 3B). Although the structures on both sides of this transition have the same monoclinic symmetry ( $Cc$ ), there is a distinct change in the ionic coordinates from a distorted version of the rhombohedral bulk structure (with octahedral coordination of the  $\text{Fe}^{3+}$  cation) to a structure with essentially five-fold coordination of the Fe cation, resembling the “super-tetragonal” structure observed for  $\text{PbVO}_3$  and  $\text{BiCoO}_3$  (26, 27) but with additional tilting of the oxygen polyhedra (see insets in Fig. 3A). The energy versus strain curve (Fig. 3A) shows a maximum separating the two lower-energy phases at around 4.5% strain, suggesting that films strained to this critical value may lower their energy by spontaneously phase-separating into the T and R phases. In this case, the two phases have in-plane lattice parameters that are smaller and larger, respectively, than that of the substrate, allowing for phase-separation without an overall change of in-plane film dimensions. Films grown at higher strain values will be in the metastable tetragonal-like phase energy minimum and are not expected to phase separate. We have investigated this experimentally by studying the evolution of the BFO films on a wide range of substrates, including (110)  $\text{DyScO}_3$  (DSO) ( $a = 3.94 \text{ \AA}$ ), STO ( $a = 3.905 \text{ \AA}$ ), (001)  $(\text{LaAlO}_3)_{0.3}(\text{SrAl}_{0.5}\text{Ta}_{0.5}\text{O}_3)_{0.7}$  (LSAT) ( $a = 3.87 \text{ \AA}$ ), LAO ( $a = 3.79 \text{ \AA}$ ), and YAO ( $a = 3.69 \text{ \AA}$ ) (all lattice parameters reported here are the cubic or pseudocubic values, and the lattice mismatch of the various substrates relative to bulk BFO is shown in Fig. 3, A and B). These studies show that BFO films on YAO consist entirely of the T phase for film thicknesses up to  $\sim 220 \text{ nm}$ , whereas films on LAO are mixed T and R phases, and films on LSAT, STO, and DSO are rhombohedral-like in nature, consistent with the theoretical predictions in Fig. 3. Phase field calculations of the strain-driven morphotropic phase

boundary, shown in fig. S5, confirm the conclusions from ab initio calculations. They also reveal the existence of the two-phase region between the tetragonal-like and rhombohedral-like phases and show the persistence of this two-phase region at finite temperature.

We probe the surface displacements and piezoelectric properties on a local scale using AFM and PFM, and we focus here on samples that exhibit a mixed T and R phase structure. An overview of the piezoelectric switching behavior for such a sample is shown in fig. S6. The AFM image (fig. S6A) shows two major topographical features: bright plateaus that we interpret to arise from the T phase and areas of stripe-like contrast that we interpret to arise from mixed T and R regions. The corresponding out-of-plane (fig. S6B) and in-plane (fig. S6C) PFM images show that there is an out-of-plane switching of the polarization upon application of an electric field, and the in-plane image shows no change in contrast, consistent with the idea that the polarization vector is primarily perpendicular to the sample surface.

We now focus on the details of the piezoelectric behavior of an 85-nm-thick mixed T and R phase sample. We have measured the normalized relative surface displacement of a local poled area as a function of electric field applied to the scanning probe tip (Fig. 4A). (Fig. S8 shows in-plane and out-of-plane PFM data corresponding to Fig. 4, B to E.) These measurements were repeated at five locations on each of five different samples to ensure repeatability. The relative displacements were measured by comparing the average height within the switched area to the entire scanned area outside the switched area. These relative displacements were then converted to strain values. The data in this figure present several interesting features: first is the observation of a “butterfly-loop,” which is typical of the strain versus field behavior that is commonly observed in piezoelectrics. At the highest fields (both positive and negative polarity), the relative deformation

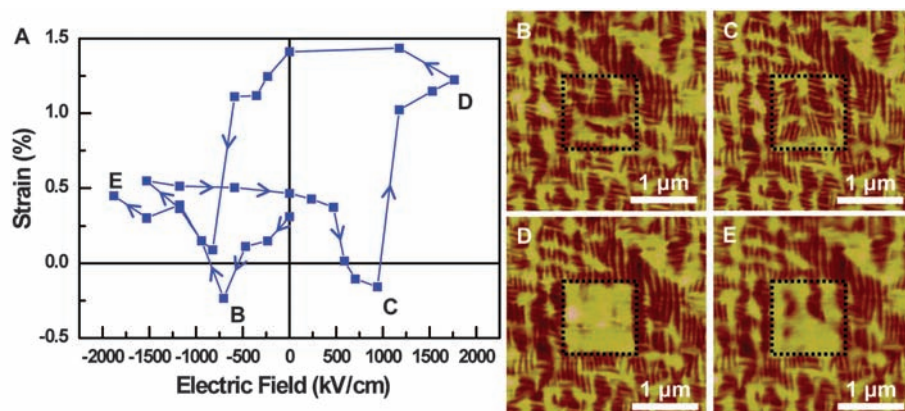


**Fig. 4.** (A) Electric field induced changes in surface displacement, here represented as strains, show a classic “butterfly” loop structure. Corresponding AFM images at (B)  $-1880 \text{ kV/cm}$ , (C)  $-705 \text{ kV/cm}$ , (D)  $1760 \text{ kV/cm}$ , and (E)  $941 \text{ kV/cm}$  are shown. At the extremes of applied voltage, a clear, single contrast is observed in the switched box corresponding to the presence of the tetragonal phase. A dashed line indicates the area that was subjected to the electric field.

is the highest; this corresponds to an essentially single-domain, tetragonal-like state of the sample, as exemplified by the uniform image contrast in the AFM images (Fig. 4, D and E). In contrast, at the lowest value of relative displacement, the AFM images (Fig. 4, B and C) show clear signatures of stripe-like image contrast, indicative of a mixed state. As shown in fig. S7, we have been able to reversibly switch it through the states shown in Fig. 4, B to D. We note that the absolute value of the local surface displacement is  $\sim 1$  to 2 nm per 85 nm of film thickness. This corresponds to an effective strain of 1.2 to 2.4%, which is of the same order of magnitude as the highest strains reported for the relaxor ferroelectrics. These relatively large and nonvolatile changes in surface displacements make this an attractive system for use in nanoscale data storage elements (such as probe-based data storage) and microscale actuators (28).

Our experimental and theoretical studies have revealed the ability of the BFO system to morph into allotropic modifications. These forms are stabilized through the epitaxial strain imposed by the substrate. Of particular interest from the piezoelectrics point of view is the mixed phase state of the films. The ability to reversibly convert the T phase to a mixture of T and R phases through the application of an electric field suggests a close resemblance to other well-known piezoelectrics such as the morphotropic phase boundary compositions in the PZT family and the PMN-PT family. Our observations support the notion that such strain-driven phase evolution is a generic feature, akin to chemically driven phase changes

that are now well established in the manganites, cuprates, and relaxors. Furthermore, the observation of the strain-driven phase changes in BFO should motivate a search for similar control in other related perovskite systems. Furthermore, this reversible interconversion is accompanied by substantial changes in the height of the sample surface (a few nanometers), thus making this potentially attractive for AFM probe-based data storage applications.

#### References and Notes

1. P. Groth, *Ann. Phys. Chem.* **217**, 31 (1870).
2. V. M. Goldschmidt, *Trans. Faraday Soc.* **25**, 253 (1929).
3. R. E. Newnham, *Mater. Res. Soc. Bull.* **22**, 20 (1997).
4. E. Dagotto, *Nanoscale Phase Separation and Colossal Magnetoresistance*, (Springer Verlag, New York, 2003).
5. S. E. Park, T. R. ShROUT, *J. Appl. Phys.* **82**, 1804 (1997).
6. R. Guo *et al.*, *Phys. Rev. Lett.* **84**, 5423 (2000).
7. H. Fu, R. E. Cohen, *Nature* **403**, 281 (2000).
8. M. Ahart *et al.*, *Nature* **451**, 545 (2008).
9. W. Eerenstein, N. D. Mathur, J. F. Scott, *Nature* **442**, 759 (2006).
10. R. Ramesh, N. A. Spaldin, *Nat. Mater.* **6**, 21 (2007).
11. C. Ederer, N. A. Spaldin, *Phys. Rev. Lett.* **95**, 257601 (2005).
12. P. Ravindran, R. Vidyaa, A. Kjekshus, H. Fjellvåg, *Phys. Rev. B* **74**, 224412 (2006).
13. D. Ricinchi, K.-Y. Yun, M. Okuyama, *J. Phys. Condens. Matter* **18**, L97 (2006).
14. H. Béa *et al.*, *Phys. Rev. Lett.* **102**, 217603 (2009).
15. D. G. Schlom *et al.*, *Annu. Rev. Mater. Res.* **37**, 589 (2007).
16. F. Zavaliche *et al.*, *Phase Transit.* **79**, 991 (2006).
17. G. Xu *et al.*, *Appl. Phys. Lett.* **86**, 182905 (2005).
18. Y. H. Chu *et al.*, *Appl. Phys. Lett.* **90**, 252906 (2007).
19. H. Béa *et al.*, *Phys. Rev. B* **74**, 020101 (2006).
20. K. Y. Yun *et al.*, *J. Appl. Phys.* **96**, 3399 (2004).
21. Materials and methods are available as supporting material on Science Online.

22. M. F. Chisholm *et al.*, *Microsc. Microanal.* **10**, 256 (2004).
23. G. Kresse, J. Furthmüller, *Phys. Rev. B* **54**, 11169 (1996).
24. V. I. Anisimov, F. Aryasetiawan, A. I. Liechtenstein, *J. Phys. Condens. Matter* **9**, 767 (1997).
25. A. G. Christy, *Acta Crystallogr. B* **51**, 753 (1995).
26. R. V. Shpanchenko *et al.*, *Chem. Mater.* **16**, 3267 (2004).
27. A. A. Belik *et al.*, *Chem. Mater.* **18**, 798 (2006).
28. S. Hong, Ed., *Nanoscale Phenomena in Ferroelectric Thin Films* (Kluwer Academic Publishing, Boston, MA, 2004).
29. The work at Berkeley is supported by the Director, Office of Science, Office of Basic Energy Sciences, Materials Sciences Division of the U.S. Department of Energy under contract DE-AC02-05CH11231. The authors from Berkeley acknowledge the support of the National Center for Electron Microscopy, Lawrence Berkeley National Laboratory. Y.H.C. also acknowledges the support of the National Science Council, R.O.C., under contract NSC 98-2119-M-009-016. V.G. and D.G.S. acknowledge support from National Science Foundation grants DMR-0820404 and DMR-0507146. A.H. and N.S. acknowledge support from the National Science Foundation under DMR-0820404 and NIRT-0609377. Theoretical work used the SGI Altix [Cobalt] system and the TeraGrid Linux Cluster [Mercury] at the National Center for Supercomputing Applications under grant DMR-0940420. C.E. acknowledges support from the Science Foundation of Ireland (grant SFI-07/Y12/I1051). The work of G.S. and L.Q.C. is supported by Department of Energy Basic Sciences under contract DE-FG02-07ER46417.

#### Supporting Online Material

www.sciencemag.org/cgi/content/full/326/5955/977/DC1  
Materials and Methods  
Figs. S1 to S8  
References

29 May 2009; accepted 1 September 2009  
10.1126/science.1177046

## Observation of the Role of Subcritical Nuclei in Crystallization of a Glassy Solid

Bong-Sub Lee,<sup>1,2</sup> Geoffrey W. Burr,<sup>3</sup> Robert M. Shelby,<sup>3</sup> Simone Raoux,<sup>3\*</sup> Charles T. Rettner,<sup>3</sup> Stephanie N. Bogle,<sup>1,2</sup> Kristof Darmawikarta,<sup>1,2</sup> Stephen G. Bishop,<sup>2,4</sup> John R. Abelson<sup>1,2,†</sup>

Phase transformation generally begins with nucleation, in which a small aggregate of atoms organizes into a different structural symmetry. The thermodynamic driving forces and kinetic rates have been predicted by classical nucleation theory, but observation of nanometer-scale nuclei has not been possible, except on exposed surfaces. We used a statistical technique called fluctuation transmission electron microscopy to detect nuclei embedded in a glassy solid, and we used a laser pump-probe technique to determine the role of these nuclei in crystallization. This study provides a convincing proof of the time- and temperature-dependent development of nuclei, information that will play a critical role in the development of advanced materials for phase-change memories.

The phase transformation of a material often starts with the formation of nanometer-sized volumes of the new phase, nuclei, which then grow in size. The nucleation process has been described by classical theory (*I-3*), in which the thermodynamic free energy is reduced by the phase transformation, whereas the formation of a nucleus involves an energy penalty associated with the boundary region between the

phases, particularly when atomic bonds are broken or strained. This interplay between volume and surface effects results in a critical nucleus size. For a subcritical nucleus, the energy rises as atoms are added to the new configuration; for a supercritical nucleus, the energy falls, because the energy reduction by phase transformation is now greater than the surface penalty. As thermal fluctuations induce atoms to join or leave each

subcritical nucleus, a size distribution of subcritical nuclei develops in the material. Only a minute fraction of subcritical nuclei achieve the critical size ( $n_c$ ) and continue to grow into a crystalline grain that is large enough to be detected by conventional analyses.

However, very few experimental studies have provided quantitative information on the distribution of nanoscale subcritical nuclei that develops before the observable phase transformation. Data are available only in very special cases, such as heteroepitaxial film growth where the nuclei are exposed on a flat surface (*4, 5*). On the micron length scale, nuclei and their behaviors can be observed in the agglomeration of colloidal particles in liquids (*6, 7*). The general case, such as crystallization from nanometer-scale nuclei that are embedded in the parent glassy phase,

<sup>1</sup>Department of Materials Science and Engineering, University of Illinois at Urbana-Champaign (UIUC), Urbana, IL 61801, USA. <sup>2</sup>Coordinated Science Laboratory, University of Illinois at Urbana-Champaign, Urbana, IL 61801, USA. <sup>3</sup>IBM/Macronix Phase Change Random Access Memory Joint Project, IBM Almaden Research Center, San Jose, CA 95120, USA. <sup>4</sup>Department of Electrical and Computer Engineering, University of Illinois at Urbana-Champaign, Urbana, IL 61801, USA.

\*Present address: IBM T. J. Watson Research Center, Yorktown Heights, NY 10598, USA.

†To whom correspondence should be addressed. E-mail: abelson@illinois.edu